ISSN 1674-1056
http://cpb.iphy.ac.cn
http://iopscience.iop.org/cpb
中国物理 B
Chinese Physics
中国物理 Chinese Physics B

Electrically triggered dual-band tunable terahertz metamaterial band-pass filter based on Si_3N_4-VO_2-Si_3N_4sandwich

Shuai Zhao(赵帅), Fangrong Hu(胡放荣), Xinlong Xu(徐新龙), Mingzhu Jiang(江明珠), Wentao Zhang(张文涛), Shan Yin(银珊), Wenying Jiang(姜文英)

Citation: Chin. Phys. B . 2019, 28(5): 054203. **doi:** 10.1088/1674-1056/28/5/054203
Journal homepage: http://cpb.iphy.ac.cn; http://iopscience.iop.org/cpb

What follows is a list of articles you may be interested in

Propagation characteristics of oblique incidence terahertz wave through non-uniform plasma

Antao Chen(陈安涛), Haoyu Sun(孙浩宇), Yiping Han(韩一平), Jiajie Wang(汪加洁), Zhiwei Cui(崔志伟)
Chin. Phys. B . 2019, 28(1): 014201. **doi:** 10.1088/1674-1056/28/1/014201

Energy scaling and extended tunability of a ring cavity terahertz parametric oscillator based on $KTiOPO_4$crystal

Yuye Wang(王与烨), Yuchen Ren(任宇琛), Degang Xu(徐德刚), Longhuang Tang(唐隆煌), Yixin He(贺奕焮), Ci Song(宋词), Linyu Chen(陈霖宇), Changzhao Li(李长昭), Chao Yan(闫超), Jianquan Yao(姚建铨)
Chin. Phys. B . 2018, 27(11): 114213. **doi:** 10.1088/1674-1056/27/11/114213

Terahertz two-pixel imaging based on complementary compressive sensing

Yuye Wang(王与烨), Yuchen Ren(任宇琛), Linyu Chen(陈霖宇), Ci Song(宋词), Changzhao Li(李长昭), Chao Zhang(张超), Degang Xu(徐德刚), Jianquan Yao(姚建铨)
Chin. Phys. B . 2018, 27(11): 114204. **doi:** 10.1088/1674-1056/27/11/114204

High efficiency terahertz diffraction grating with trapezoidal elements

Yin-Zhong Wu(巫殷忠), Quan-Pin Fan(范全平), Qiang-Qiang Zhang(张强强), Lai Wei(魏来), Yong Chen(陈勇), Zu-Hua Yang(杨祖华), Lei-Feng Cao(曹磊峰)
Chin. Phys. B . 2017, 26(12): 124203. **doi:** 10.1088/1674-1056/26/12/124203

Mechanically tunable metamaterials terahertz dual-band bandstop filter

Fangrong Hu(胡放荣), Xin Xu(胥欣), Peng Li(李鹏), Xinlong Xu(徐新龙), Yue'e Wang(王月娥)
Chin. Phys. B . 2017, 26(7): 074219. **doi:** 10.1088/1674-1056/26/7/074219

Electrically triggered dual-band tunable terahertz metamaterial band-pass filter based on Si_3N_4–VO_2–Si_3N_4 sandwich*

Shuai Zhao(赵帅)[1], Fangrong Hu(胡放荣)[1,†], Xinlong Xu(徐新龙)[2], Mingzhu Jiang(江明珠)[1], Wentao Zhang(张文涛)[1], Shan Yin(银珊)[1], and Wenying Jiang(姜文英)[1]

[1] *Guangxi Key Laboratory of Optoelectronic Information Processing, Guilin University of Electronic Technology, Guilin* 541004, *China*

[2] *Nanobiophotonic Center, State Key Laboratory Incubation Base of Photoelectric Technology and Functional Materials, and Institute of Photonics & Photon-Technology, Northwest University, Xi'an* 710069, *China*

(Received 21 December 2018; revised manuscript received 17 January 2019; published online 20 March 2019)

We experimentally demonstrate an electrically triggered terahertz (THz) dual-band tunable band-pass filter based on Si_3N_4–VO_2–Si_3N_4 sandwich-structured hybrid metamaterials. The insulator–metal phase transition of VO_2 film is induced by the Joule thermal effect of the top metal layer. The finite-integration-time-domain (FITD) method and finite element method (FEM) are used for numerical simulations. The sample is fabricated using a surface micromachining process, and characterized by a THz time-domain-spectrometer (TDS). When the bias current is 0.225 A, the intensity modulation depths at two central frequencies of 0.56 THz and 0.91 THz are about 81.7% and 81.3%, respectively. This novel design can achieve dynamically electric–thermo–optic modulation in the THz region, and has potential applications in the fields of THz communications, imaging, sensing, and astronomy exploration.

Keywords: tunable band-pass filter, hybrid metamaterials, terahertz, vanadium dioxide (VO_2)

PACS: 42.79.Ci, 81.05.Xj, 84.30.Vn **DOI:** 10.1088/1674-1056/28/5/054203

1. Introduction

Metamaterials (MMs) are artificially constructed electromagnetic (EM) materials and media which have exotic EM responses that are unavailable in nature. Consequently, they have many applications, such as negative refractive index,[1] cloaking,[2] superlenses,[3] optical switching,[4] absorbers,[5] modulators,[6] and thermal emitters.[7]

Recently, many THz filters based on the MMs have been proposed; for example, a modified four-split complementary structure MM was used to construct a dual-band band-pass filter with central frequencies centered at 0.315 TH and 0.48 THz,[8] respectively. In addition, an ultra-broad THz band-pass filter based on metal–dielectric–metal sandwich structure was presented.[9] It should be noted that neither can be actively tuned and modulated.

However, in many practical applications, tunable THz filters are greatly needed. Thus, they have become a research focus over the past decade, and many tunable THz MMs filters which utilize optical,[10] electrical,[11] and mechanical[12] stimuli to reconfigure the MMs' structures have been reported. For all these active stimuli, the optical stimulus requires an external optical source, which increases the system's complexity and alignment difficulty. The electrical stimulus method has good compatibility with the integration circuit (IC) process, but its modulation depth is not very high and sometimes shows distinct resonance frequency shift. The mechanical stimulus usually contains some movable micromechanical segments, can achieve high modulation depth, and has good compatibility with the IC process, but its fabrication is complex and expensive.

Recently, more attention has been focused on the thermal stimulus[13–15] method, which usually uses phase-transition materials (i.e., VO_2) to reconfigure the MMs and achieves a very high modulation depth and a broad modulation bandwidth, because VO_2 shows the insulator phase at a low temperature and the metal phase above the critical temperature about $T_c = 340$ K.[16,17]

In a recent work,[18] demonstrated a broadband on/off filter using frequency selection surface and VO_2. However, an external heater was required to induce the phase transition of the whole VO_2 layer, which was very difficult for integration, and the time for the phase transition of VO_2 is very long. In another work,[19] a THz modulator with a modulation depth of 87% and a bandwidth of 0.7 THz was proposed but the maximum bias current of 0.5 A is still too high for many applications. In addition, an electrically voltage driven THz modulator based on a hybrid bowtie-antenna-VO_2 device was proposed for modulating the THz wave in a wide frequency range of 0.3 THz to 2.5 THz.[20] However, the maximum modulation depth is smaller than 81%. Therefore, the tunable THz filters

*Project supported by the National Natural Science Foundation of China (Grant Nos. 11574059, 61565004, and 11774288), the National Technology Major Special Project, China (Grant No. 2017ZX02101007-003), the Natural Science Foundation of Guangxi, China (Grant Nos. 2015GXNSFDA139039 and 2017GXNSFBA198116), the Foundation from Guangxi Key Laboratory of Automatic Detection Technology and Instrument, China (Grant No. YQ16101), and the Innovation Project of Guangxi Graduate Education, China (Grant Nos. 2018YJCX70, 2018YJCX67, and 2018YJCX74).

†Corresponding author. E-mail: hufangrong@sina.com

© 2019 Chinese Physical Society and IOP Publishing Ltd

with low driven current (or voltage) and high modulation depth are very important for integration.

In this work, we propose an electrically triggered dual-band tunable THz band-pass filter based on the Si_3N_4–VO_2–Si_3N_4 sandwich-structured hybrid MMs. By introducing a closed ring and two split ring resonators (SRRs) in a unit cell, three absorption peaks are produced at the frequencies of 0.37 THz, 0.78 THz, and 1.03 THz, just by forming two pass-bands between these absorption peaks. The full width at half maximum (FWHM) of the first and that of the second pass-band are 0.29 THz and 0.2 THz, respectively. Unlike other VO_2-based tunable THz filters,[18–20] the tunable filter proposed in this work has three advantages. First, it has good ability for resisting the thermal stress due to the use of Si_3N_4–VO_2–Si_3N_4 sandwiched structure. Second, it is fully electrically triggered and has good compatibility with the IC process. Finally, it can achieve high modulation depth at very low bias currents.

2. Design and fabrication

A schematic diagram of the unit cell is shown in Fig. 1(a). From bottom to top, there are 650 μm thick high resistance silicon substrate, 100 nm thick Si_3N_4 layer, 125 nm thick VO_2 phase-transition layer, 500 nm thick Si_3N_4 layer, and 100 nm thick aluminum pattern layer (which is used for the frequency selection and the electrical connection). The lower layer of Si_3N_4 is used as a buffer layer, while the upper layer of Si_3N_4 has three functions. First, it is used as an electrical isolation layer between the top metal layer and the VO_2 layer. Second, it works as a heat transfer layer to lower the loss of VO_2 at room temperature. Finally, it is served as a diffusion barrier that allows crystallization of the VO_2 layer. When the external current is applied, the Joule heat produced in the metal layer could induce the insulator–metal phase transition of the VO_2 layer. Due to the good ability of Si_3N_4 to resist thermal stress, this device has good thermal stability. In addition, low current is required to produce the phase transition in the VO_2 layer, because the aluminum has good electrical conductivity and thermal conductivity.

The top view of a unit cell is illustrated in Fig. 1(b), which contains a closed ring and two split-ring-resonators, and all optimized dimensions of the unit cell are listed in Table 1.

Table 1. Optimized dimensions of a unit cell (μm).

w_1	w_2	w_3	L_1	L_2	p_x	p_y	g_1	g_2
2	3	3	66	48	90	90	10	6

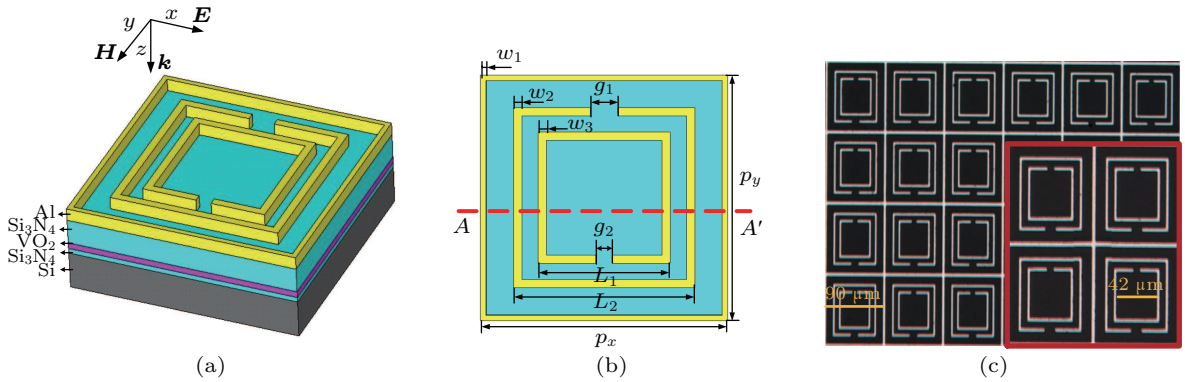


Fig. 1. Schematic diagrams of the device. (a) Oblique view of a unit cell, (b) top view of a unit cell, and (c) microscopy image of the sample.

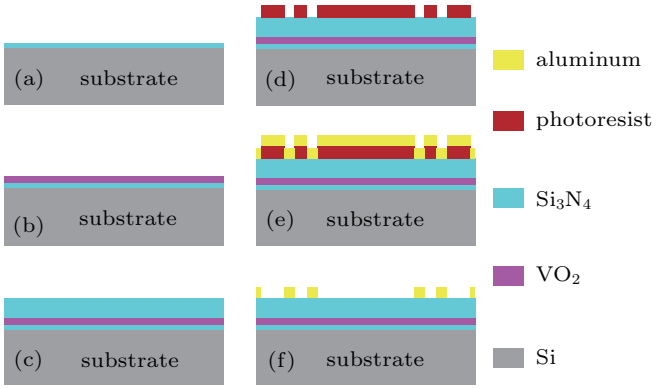


Fig. 2. The fabrication process flow.

The sample is fabricated by a surface micromachining process. The process begins with a double-sided polished high resistance silicon wafer, and the process flow is illustrated in Fig. 2. First, in Fig. 2(a), a layer of 100 nm Si_3N_4 is deposited on the high resistance silicon wafer by using plasma enhanced chemical vapor deposition (PECVD) process; second, in Fig. 2(b), a layer of 125 nm VO_2 is deposited using magnetron sputtering method and then annealed at 450 degrees; after that, in Fig. 2(c), the second layer of Si_3N_4 with the thickness of 500 nm is deposited using the PECVD process; then, in Fig. 2(d), negative photoresist is spin-coated and lithographically patterned, and then developed; after that, in Fig. 2(e), a metal stack consisting of 10 nm chrome and 100 nm aluminum is deposited over the photoresist pattern by e-beam evaporation; finally, in Fig. 2(f), the photoresist is dissolved using lift-off process and leave behind the metal in the

opened areas. The microscopy image of the fabricated sample is shown in Fig. 1(c).

3. Numerical simulation and optical characterization

Microwave Studio 2016, which is a commercial software computer simulation technology (CST), is used to implement a full-wave electromagnetic simulation to compute and optimize the transmission properties of the device. In the simulation, an open boundary condition is set in the z direction, and unit cell boundary conditions are set in the x and y directions, respectively. An adaptive mesh refinement is used in the frequency solver, and a classical Drude model[21] is introduced to define the properties of the VO_2 film, in which the relative permittivity of VO_2 in the THz region is described as

$$\varepsilon(\omega) = \varepsilon_\infty - \frac{\omega_p^2(\sigma)}{\omega^2 + i\gamma\omega}, \tag{1}$$

where the relative permittivity at high frequency $\varepsilon_\infty = 12$, $\omega_p(\sigma)$ is the conductivity-dependent plasma frequency, and γ is the collision frequency. Both the conductivity σ and $\omega_p^2(\sigma)$ are proportional to the density of free carriers in the VO_2 film; thus, the plasma frequency can be expressed as

$$\omega_p^2(\sigma) = \frac{\sigma}{\sigma_0}\omega_p^2(\sigma_0), \tag{2}$$

where $\sigma = 3 \times 10^5$ S/m, $\omega_p(\sigma) = 1.4 \times 10^{15}$ rad/s, and $\gamma = 5.75 \times 10^{13}$ rad/s. These parameters agree well with the reported experimental results.[22] The layer of Si_3N_4 is modeled as a normal dielectric with a complex permittivity of $\varepsilon = 7 + i2.86$. The metal aluminum is modeled as a lossy metal with an electrical conductivity $\sigma_m = 3.56 \times 10^7$ S/m. Figure 3 presents the schematic of the bias method in the test experiment.

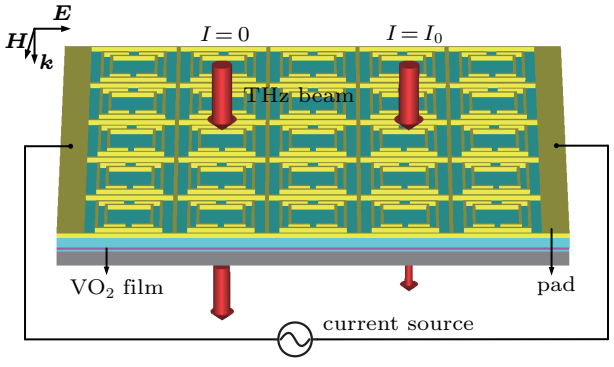


Fig. 3. A schematic diagram of the bias method in the test experiment. All closed rings are connected to the two pads on both sides and biased with a current source. The phase transition is induced by the Joule heating of the metal pattern. The red arrows represent the intensities of the THz wave under different bias currents.

In the simulation, to investigate the phase transition of the VO_2 layer, we change its conductivity and calculate the transmission spectra of the device (Fig. 4(a)). The black solid curve represents the transmission without bias current ($I = 0$), which shows three intensive resonance absorption peaks at 0.38 THz, 0.73 THz, and 0.96 THz, respectively. The maximum transmissions at the central frequencies of two passbands, i.e., 0.59 THz and 0.86 THz, are 84.2% and 80.6%, respectively. When the conductivity of the VO_2 layer increases from the minimum of 12 S/m to the maximum of 3×10^5 S/m, the transmission of the device decreases gradually from the maximum to near zero, and the corresponding modulation depth achieves about 100%.

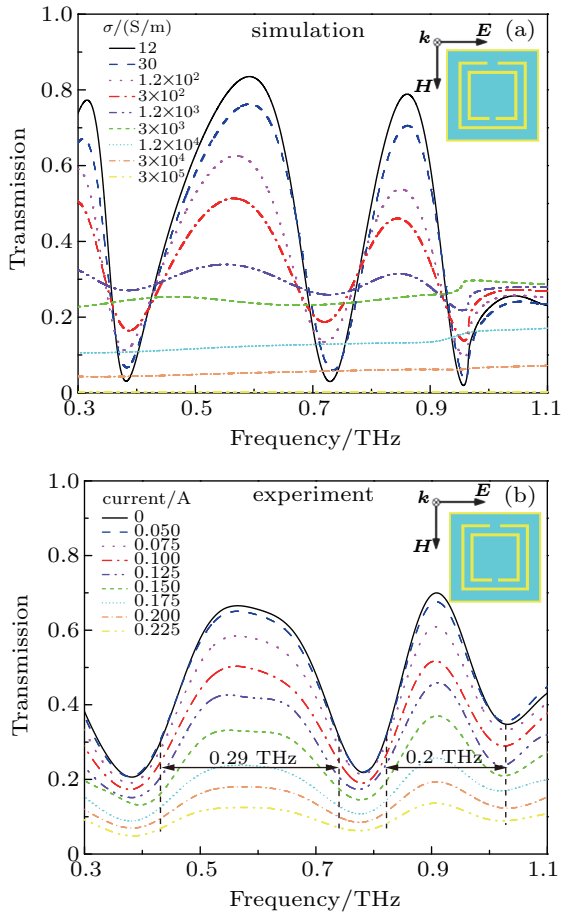


Fig. 4. Simulation and experiment results. (a) Simulated transmissions for different conductivity of the VO_2 layer. (b) Measured transmissions for different bias currents.

In the experiment, the bias currents are supplied with a direct power supply. When the bias currents are applied, the transmissions are measured using a THz time-domain spectrum system (Z-3 model, Zomega Corp.)[23] and plotted in Fig. 4(b). When the bias current increases from zero to 0.225 A, the transmission gradually decreases from the maximum to about 0.1. The full width at half maximum (FWHM) of the first passband and that of the second one are 0.29 THz and 0.2 THz, respectively. The experiment shows good agreement with the simulation.

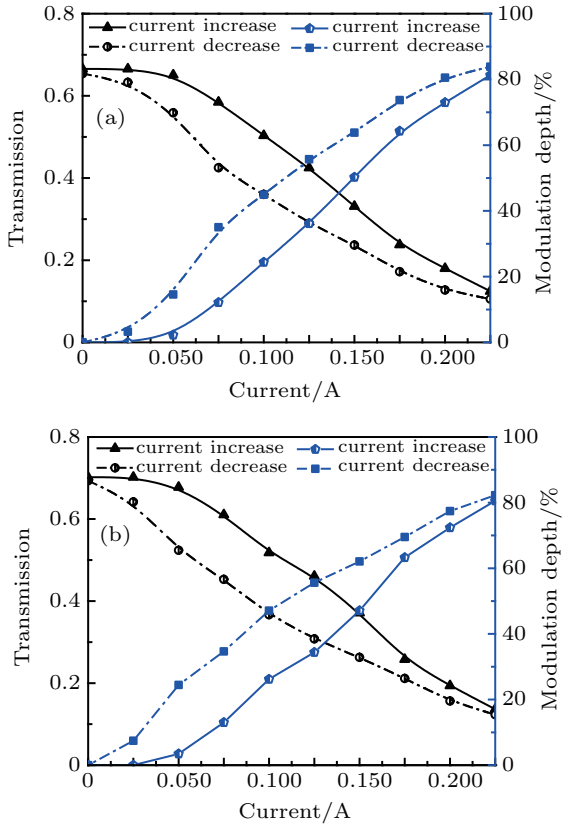


Fig. 5. Hysteresis behavior and modulation depth. (a) Hysteresis behavior and modulation depth at the central frequency of the first band ($f = 0.56$ THz). (b) Hysteresis behavior and modulation depth at the central frequency of the second band ($f = 0.91$ THz).

To understand the modulation characteristics of the device, we have defined the modulation depth as $M_{\rm d} = (|T_0 - T|/T_0) \times 100\%$, where T_0 and T are the transmission without current and the transmission with practical bias currents, respectively. The calculated results extracted from Fig. 4(b) are presented in Figs. 5(a) and 5(b), showing that the measured maximum transmission at the two central frequencies (i.e., 0.56 THz and 0.91 THz) of two passbands are 68.2% and 70.4%, respectively. Moreover, the maximum modulation depths of 0.56 THz and 0.91 THz are 81.7% and 81.3%, respectively. The fine tuning capability of the sample is attributed to the gradual thermal-induced phase transition of the VO_2 film. The differences between the simulation and the experiment are probably derived from the fabrication process, which results in the practical values of the material parameters being different from those used in the simulation.

In addition, as shown in Figs. 5(a) and 5(b), a distinct hysteresis behavior is observed when the applied currents go up and down.

4. Physical mechanism

To understand the physical mechanism of the device, the surface currents distributed on the aluminum film at three absorption frequencies are plotted in Fig. 6.

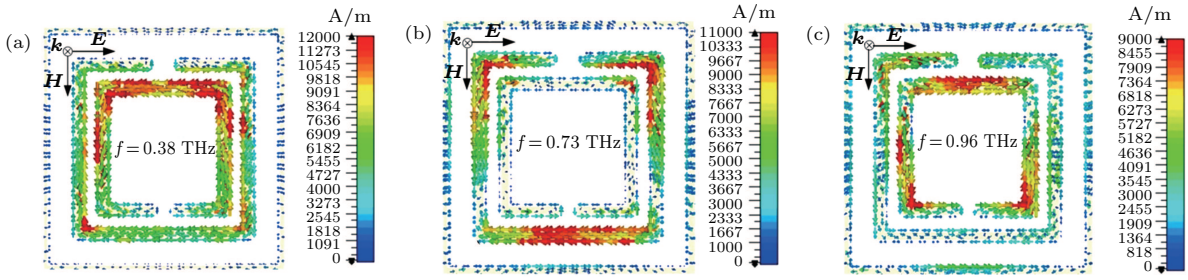


Fig. 6. Surface currents distributed on the top patterned aluminum film for three absorption frequencies: (a) $f = 0.38$ THz, (b) $f = 0.73$ THz, and (c) $f = 0.96$ THz.

Figure 6(a) shows that the first absorption peak at the resonant frequency of $f = 0.38$ THz is mainly produced by the surface currents oscillating on the inner SRR, which is a typical inductive–capacitive (LC) resonance mode.[24] As shown in Fig. 6(b), the surface currents mainly oscillate on the outer SRR and they are typical tri-pole resonance. Two of them on the upper section of the SRR have the same phase which is reverse to the phase of another one on the bottom of the SRR. Therefore, the second resonant frequency $f = 0.73$ THz is excited by this tri-pole resonance. Figure 6(c) indicates that the third absorption peak at $f = 0.96$ THz is similar to the second one, and it is produced by the tri-pole resonance on the inner SRR.

To investigate the steady-state temperature distribution and the Joule heating performance of the device, we implement an electrical–thermal simulation by using finite element analysis (FEM) software, COMSOL multiphysics 5.3a.[25] The material parameters of Al, Si, and Si_3N_4 are taken from the default textbook,[26] where the heat capacity, the thermal conductivity, and the density of VO_2 film are set as 706.25 J/(kg·K), 6.7 W/(m·K), and 4571 kg/m^3,[27] respectively. The Joule heating effect is simulated by coupling an electric currents (EC) physics model to a heat transfer (HT) in solid physics model. The right pad is set to ground and the left pad is set to the current terminal excitation with a parametric sweep. To simulate actual heat radiation, the boundaries of the model are set to diffuse surfaces with an initial temperature of $T = 293.15$ K.

Figure 7(a) presents the relationship between the peak temperature of the device at the thermal steady-state and

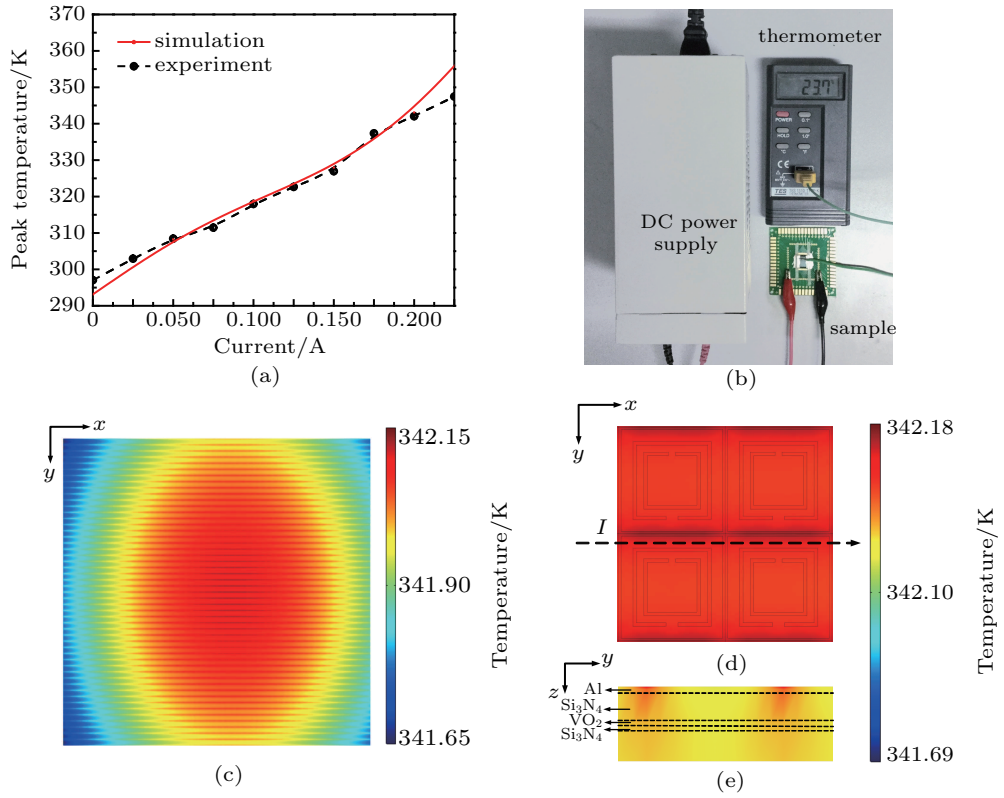


Fig. 7. Electrical–thermal characteristics. (a) The relationship between peak temperature of the device and the applied currents. (b) Temperature distributions on VO_2 film for $I = 0.2$ A. (c) Temperature distributions on four unit cells for $I = 0.2$ A. (d) Temperature distributions on the cross section of a unit cell for $I = 0.2$ A.

the applied currents. The red-solid curve is obtained by the electrical–thermal FEM simulation, and the black dashed curve is obtained from the experiment. In the simulation, the temperature of the device at thermal steady-state is 342.18 K for $I = 0.2$ A, which shows very little difference from the experiment result of 342.05 K. Meanwhile, the phase transition temperature in the simulation is consistent with the first order phase transition temperature of $T_c = 340$ K. In the temperature test experiment, a thermometer with a touching point detector is used to test the temperature on the surface of the filter, as shown in Fig. 7(b).

Figure 7(c) illustrates the temperature distribution on the VO_2 layer for $I = 0.2$ A, which shows that the maximum and the minimum temperatures of the VO_2 layer at the thermal steady-state are 342.15 K and 341.65 K, respectively. Meanwhile, it is evident that the temperature difference between the center and the margin of VO_2 layer is less than 0.5 degrees.

Figure 7(d) presents the steady-state temperature on the surface of the four unit cells, which shows that the maximum temperature distributes on the horizontal beam of the closed ring, because the bias currents just flow through it. Due to the driven currents flow through the sample from left to right, the temperature distribution is not symmetric about the center.

At the same time, figure 7(e) shows the temperature distributions on the cross section of a unit cell, indicating that there is very little difference on the cross section of the device. This could be attributed to the good heat transfer ability of the Si_3N_4 layer.

5. Conclusions

We have experimentally demonstrated a fully electrically triggered THz dual-band tunable band-pass filter based on the Si_3N_4–VO_2–Si_3N_4 sandwich-structured hybrid MMs. The insulator–metal phase transition of the VO_2 film is induced by the Joule thermal effect of the top metal pattern. When the bias current is 0.225 A, the modulation depths at the central frequencies of two bands, i.e., 0.56 THz and 0.91 THz, reach 81.7% and 81.3%, respectively. In particular, the central frequency of each band can be tuned to the desired frequency by only changing the geometries of the unit cell. This design paves a new way to develop fully electrically controlled THz functional devices. Therefore, it has broad applications in the field of THz communication, imaging, sensing, and astronomy exploration.

References

[1] Shelby R A, Smith D R and Schultz S 2001 *Science* **292** 77
[2] Kante B, de Lustrac A, Lourtioz J M and Burokur S N 2008 *Opt. Express* **16** 9191
[3] Silveirinha M G, Medeiros C R, Fernandes C A and Costa J R 2010 *Phys. Rev. B* **81** 033101
[4] Olivares I, Sanchez L, Parra J, Larrea R, Griol A, Menghini M, Homm P, Jang L W, van Bilzen B, Seo J W, Locquet J P and Sanchis P 2018 *Opt. Express* **26** 12387

[5] Song Z Y, Wang K, Li J W and Liu Q H 2018 *Opt. Express* **26** 7148
[6] Shi Z W, Cao X X, Wen Q Y, Wen T L, Yang Q H, Chen Z, Shi W S and Zhang H W 2018 *Adv. Opt. Mater.* **6** 1700620
[7] Liu X L, Tyler T, Starr T, Starr A F, Jokerst N M and Padilla W J 2011 *Phys. Rev. Lett.* **107** 045901
[8] Lan F, Yang Z Q, Qi L M, Gao X and Shi Z J 2014 *Opt. Lett.* **39** 1709
[9] Chiang Y J, Yang C S, Yang Y H, Pan C L and Yen T J 2011 *Appl. Phys. Lett.* **99** 191909
[10] Deng L, Li D Z, Liu Z L, Meng Y H, Guo X N and Tian Y H 2017 *Chin. Phys. B* **26** 024209
[11] Chen H T, Padilla W J, Zide J M O, Gossard A C, Taylor A J and Averitt R D 2006 *Nature* **444** 597
[12] Hu F R, Xu X, Li P, Xu X L and Wang Y 2017 *Chin. Phys. B* **26** 074219
[13] Zhu Y H, Vegesna S, Zhao Y, Kuryatkov V, Holtz M, Fan Z Y, Saed M and Bernussi A A 2013 *Opt. Lett.* **38** 2382
[14] Park D J, Shin J H, Park K H and Ryu H C 2018 *Opt. Express* **26** 17397
[15] Hogue M N F, Karaoglan-Bebek G, Holtz M, Bernussi A A and Fan Z Y 2015 *Opt. Commun.* **350** 309
[16] Pashkin A, Kuebler C, Ehrke H, Lopez R, Halabica A, Haglund R F Jr., Huber R and Leitenstorfer A 2011 *Phys. Rev. B* **83** 195120
[17] Eaton M, Catellani A and Calzolari A 2018 *Opt. Express* **26** 5342
[18] Sanphuang V, Ghalichechian N, Nahar N K and Volakis J L 2016 *IEEE Trans. Terahertz Sci. Technol.* **6** 583
[19] Zhou G C, Dai P H, Wu J B, Jin B B, Wen Q Y, Zhu G H, Shen Z, Zhang C H, Kang L, Xu W W, Chen J and Wu P H 2017 *Opt. Express* **25** 17322
[20] Han C R, Parrott E P J, Humbert G, Crunteanu A and Pickwell-MacPherson E 2017 *Sci. Rep.* **7** 12725
[21] Wang S X, Kang L and Werner D H 2017 *Sci. Rep.* **7** 4326
[22] Zhu Y H, Zhao Y, Holtz M, Fan Z and Bernussi A A 2012 *J. Opt. Soc. Am. B: Opt. Phys.* **29** 2373
[23] Hu F R, Zhang L H, Xu X L, Wang Y E, Zou T B and Zhang W T 2015 *Opt. Quan. Electron.* **47** 2867
[24] Azad A K, Taylor A J, Smirnova E and O'Hara J F 2008 *Appl. Phys. Lett.* **92** 011119
[25] COMSOL Inc., https://www.comsol.com [2019-01-17]
[26] Haynes W M 2014 *CRC Handbook of Chemistry and Physics* (Boca Raton: CRC Press)
[27] Gopalakrishnan G, Ruzmetov D and Ramanathan S 2009 *J. Mater. Sci.* **44** 5345